

# Unsteady behavior and thermochemical non equilibrium effects in hypersonic double-wedge flows

Davide Ninni<sup>a,\*</sup>, Francesco Bonelli<sup>a,c</sup>, Gianpiero Colonna<sup>b</sup>, Giuseppe Pascazio<sup>a</sup>

<sup>a</sup>*DMMM & CEMeC, Politecnico di Bari, Via Re David 200, Bari, 70125, Italy*

<sup>b</sup>*CNR-ISTP, Via Amendola 122/D, Bari, 70126, Italy*

<sup>c</sup>*Aeronautics and Aerospace Department, von Karman Institute for Fluid Dynamics,  
B-1640 Sint-Genesius-Rode, Belgium*

---

## Abstract

The paper presents highly detailed two-dimensional numerical simulations of hypersonic nitrogen and air flows around a double wedge, characterized by a complex shock wave/boundary layer interaction (SWBLI). The aim of the study is on one hand to investigate the unsteady behavior of such an interaction and on the other to evaluate thermo-chemical non-equilibrium effects. Two different thermo-physical models have been considered, the classical multi-temperature, or mode approximation, and the state-to-state vibrational kinetics. It is shown that for the geometric configuration under investigation, the occurrence of unsteady periodic behavior depends on the flow conditions and is inhibited in the high enthalpy case. Furthermore, non-equilibrium effects become relevant in the case of high enthalpy flows and discrepancies between the results obtained with the two models are observed.

*Keywords:* Hypersonic flows, Thermochemical non-equilibrium, Double-wedge, Shock wave/boundary layer interaction, Periodic flows

---

\*Corresponding author

Email addresses: [davide.ninni@poliba.it](mailto:davide.ninni@poliba.it) (Davide Ninni), [francesco.bonelli@poliba.it](mailto:francesco.bonelli@poliba.it) (Francesco Bonelli), [gianpiero.colonna@cnr.it](mailto:gianpiero.colonna@cnr.it) (Gianpiero Colonna), [giuseppe.pascazio@poliba.it](mailto:giuseppe.pascazio@poliba.it) (Giuseppe Pascazio)

## 1. Introduction

Nowadays, the study of hypervelocity flows is one of the strongholds of atmospheric entry and hypersonic flights. At high enthalpy regime, the temperature reaches very high values ( $>10000$  K) leading to extremely challenging thermo-  
chemical conditions, hard to be sustained by a body entering in the atmosphere.  
Therefore, experimental and numerical investigations are required in order to provide accurate predictions of aerodynamics and thermal loads on a body flying at hypersonic speed [1]. Moreover, the presence of shock wave/boundary layer interactions makes these flows even more difficult to treat, also due to unsteady phenomena occurrence. Several configurations can be accounted for:  
double-wedge geometries are particular interesting since they represent a simplified reproduction of aircraft components such as fuselage or wings [2–7].

By the time, several experiments have been carried out: Swantek and Austin [3] took advantage of a diagnostic setup to collect Schlieren images at different snapshots. Several flow regimes were analyzed and it has been shown that these flows are generally non-stationary. Recently, Durna and Celik [8] demonstrated that the nature of the non-stationarity strongly depends on the value of the aft-angle  $\theta_2$ , keeping a constant value of the fore-angle  $\theta_1$  (see geometry in fig.1). Specifically, the flow is time periodic for  $\theta_2 > 47$  degrees. Nevertheless, their analysis was limited to a nitrogen mixture in low enthalpy regime. Vatansever and Celik [9] extended this analysis by demonstrating that the aft angle affects also chemical dissociation phenomena, when non-equilibrium is relevant (high enthalpy regime). In 2017, an extended research activity, involving many researchers of different institutions, provided important numerical and experimental results [4] predicting heat transfer peak within the experimental uncertainty and reaching the conclusion that non-equilibrium effects were unimportant for low enthalpy regimes.

The development of hypersonic flight vehicles recently increased the interest towards double wedge problem in high enthalpy conditions, where aerothermodynamics is characterized by a major impact of non-equilibrium on the macro-

scopic flow features. Indeed, thermal and chemical relaxation times are of the same order of the fluid dynamics time scale leading to thermochemical non-equilibrium. In these conditions, an accurate model should be able to account for energy exchange, among and inside each vibrational mode of molecules, as well as for chemical reactions. A recent work by Reinert et al. [2], investigating the effects of non-equilibrium in the double wedge configuration, presents results of 3D numerical simulations of nitrogen flow, showing that non-equilibrium is important only for high enthalpy regimes. Moreover, flow unsteadiness has been observed even if a complete analysis to capture a periodic behavior is not provided. On the other hand, a detailed experimental and numerical analysis of air flow was carried out by Hao et al. [10] reporting Schlieren contours collected to capture instantaneous shock structures. The numerical simulations provided the prediction of flow properties at the wall.

The present paper is focused on two different aspects of the flow around a double-wedge. The first one investigates the non-stationarity of the flow for low and high enthalpy regimes, looking for a periodic behavior both for pure nitrogen and air mixtures.

Secondly, two different thermo-chemical models, namely, the well-known multitemperature model proposed by Park [11] and the state-to-state (StS) model [12], have been employed. The first model includes 5 species ( $N_2$ ,  $O_2$ ,  $NO$ ,  $N$ ,  $O$ ) and 17 chemical reactions, assuming a Boltzmann distribution for the vibrational levels at the vibrational temperature  $T_v$ . In order to account for the influence of thermal non-equilibrium on chemical reactions, the rates are evaluated at an effective temperature calculated as the geometrical mean of roto-translational temperature,  $T$ , and  $T_v$ . However, the assumption of a Boltzmann distribution is not always suitable. Indeed, it has been demonstrated (see for example Refs.[13–15]) that downstream of shocks, in supersonic expansion waves and in the boundary layer of an atmospheric entering vehicle [16–18], vibrational distributions depart from the Boltzmann one strongly affecting reaction rates and, consequently, the flow features. In this scenario, the StS model provides a powerful tool to better emulate the distribution of the molecules among all the

vibrational levels. Despite its high accuracy, this model presents a high computational cost, since molecular nitrogen and oxygen are composed of 68 and 47 vibrational levels respectively, leading to a 118 pseudo species gas mixture  
65 and more than 10000 reactions. In this context, recent studies have highlighted the importance of taking advantage of GPUs clustering, especially for very fine grids [19–21]; thus an MPI-CUDA approach is employed to drastically reduce the computational cost.

## 2. Methodology

### 70 2.1. Governing equations

Dealing with high temperature flows in the continuum regime, the classical Navier-Stokes equations have to be extended to take into account thermochemical non-equilibrium. The governing equations can be written in a compact form as follows:

$$\int_{V_0} \frac{\partial}{\partial t} \mathbf{U} dV + \oint_{S_0} \mathbf{F} \cdot \mathbf{n} dS = \int_{V_0} \mathbf{W} dV \quad (1)$$

where  $\mathbf{U}$ ,  $\mathbf{F}$  and  $\mathbf{W}$  represent the vectors of conservative variables, fluxes and source terms, respectively. In the two-dimensional case, they read:

$$\mathbf{U} = \begin{bmatrix} \rho_{1,1} \\ \vdots \\ \rho_{1,V_1} \\ \vdots \\ \rho_{N_s,V_{N_s}} \\ \rho u \\ \rho v \\ \rho e \\ \rho_{N_2} \varepsilon_{vib,N_2} \\ \rho_{O_2} \varepsilon_{vib,O_2} \\ \rho_{NO} \varepsilon_{vib,NO} \end{bmatrix} \quad (2a)$$

$$\mathbf{F} = (\mathbf{F}_E - \mathbf{F}_V, \mathbf{G}_E - \mathbf{G}_V) \quad (2b)$$

$$\mathbf{F}_E = \begin{bmatrix} \rho_{1,1} u \\ \vdots \\ \rho_{1,V_1} u \\ \vdots \\ \rho_{N_s, V_{N_s}} u \\ \rho u^2 + p \\ \rho u v \\ (\rho e + p) u \\ \rho_{N_2} \varepsilon_{vib, N_2} u \\ \rho_{O_2} \varepsilon_{vib, O_2} u \\ \rho_{NO} \varepsilon_{vib, NO} u \end{bmatrix} \quad \mathbf{G}_E = \begin{bmatrix} \rho_{1,1} v \\ \vdots \\ \rho_{1,V_1} v \\ \vdots \\ \rho_{N_s, V_{N_s}} v \\ \rho u v \\ \rho v^2 + p \\ (\rho e + p) v \\ \rho_{N_2} \varepsilon_{vib, N_2} v \\ \rho_{O_2} \varepsilon_{vib, O_2} v \\ \rho_{NO} \varepsilon_{vib, NO} v \end{bmatrix} \quad (2c)$$

$$(\mathbf{F}_V, \mathbf{G}_V) = \begin{bmatrix} -\rho_{1,1} \mathbf{u}_{1,1}^D \\ \vdots \\ -\rho_{1,V_1} \mathbf{u}_{1,V_1}^D \\ \vdots \\ -\rho_{N_s, V_{N_s}} \mathbf{u}_{N_s, V_{N_s}}^D \\ \boldsymbol{\sigma} \\ \mathbf{u} \cdot \boldsymbol{\sigma} - \mathbf{q} \\ -\mathbf{q}_{vib, N_2} \\ -\mathbf{q}_{vib, O_2} \\ -\mathbf{q}_{vib, NO} \end{bmatrix} \quad (2d)$$

$$\mathbf{W} = [\dot{\omega}_{1,1}, \dots, \dot{\omega}_{1,V_1}, \dots, \dot{\omega}_{N_s, V_{N_s}}, 0, 0, 0, \dot{\omega}_{vib, N_2}, \dot{\omega}_{vib, O_2}, \dot{\omega}_{vib, NO}]^T \quad (2e)$$

where  $u$  and  $v$  are the velocity components,  $p$  is the pressure,  $e$  is the total energy per unit mass, and the subscripts  $E$  and  $V$  stand for inviscid and viscous fluxes, while  $\mathbf{F}$  and  $\mathbf{G}$  indicate the fluxes along the  $x$  and  $y$  directions respectively.

Here, the continuity equation is substituted by a series of species continuity equations:  $N_s = 5$  is the number of species and  $V_s$  is the number of vibrational levels considered for the species  $s$ . For the Park model only the ground state is considered for vibrational modes, leading to 5 continuity equations; for the StS model  $V_{N_2} = 68$ ,  $V_{O_2} = 47$  and  $V_{NO} = V_N = V_O = 1$ , for a total of 118 continuity equations since each vibrational level is treated as a singular species. On the other hand, in order to take into account non-equilibrium phenomena, the multitemperature approach solves three additional vibrational energy equations for the molecules, with  $\varepsilon_{vib,m}$  being the vibrational energy of the molecule  $m$ . In the governing equations the viscous stress tensor ( $\boldsymbol{\sigma}$ ) and the total and vibrational heat fluxes ( $\mathbf{q}$  and  $\mathbf{q}_{vib}$ ) are evaluated as follows:

$$\boldsymbol{\sigma} = \mu \left[ \nabla \mathbf{u} + (\nabla \mathbf{u})^T \right] - \frac{2}{3} \mu (\nabla \cdot \mathbf{u}) \mathbf{I} \quad (3a)$$

$$\mathbf{q} = -\lambda_t \nabla T - \sum_{m=1}^{N_m} \lambda_{vib,m} \nabla T_{vib,m} + \sum_{s=1}^{N_s} \sum_{l=1}^{V_s} h_{s,l} \rho_{s,l} \mathbf{u}_{s,l}^D \quad (3b)$$

$$\mathbf{q}_{vib,m} = -\lambda_{vib,m} \nabla T_{vib,m} + \varepsilon_{vib,m} \rho_m \mathbf{u}_m^D \quad (3c)$$

$N_m = 3$  being the number of molecules. Here, the transport properties are indicated with  $\mu$  (mixture viscosity),  $\lambda_t$  (translational conductivity of the mixture) and  $\lambda_{vib,m}$  (vibrational conductivity of each molecule), while the enthalpy of each species is indicated with  $h_s$ . Finally, one can evaluate the diffusive velocities  $\mathbf{u}_{s,l}^D$  of the species  $s$  in the level  $l$  by using Fick's law:

$$\rho_{s,l} \mathbf{u}_{s,l}^D = -\rho D_s \nabla Y_{s,l} + \mathbf{V}_c \quad (4)$$

where  $\rho_{s,l}$  and  $Y_{s,l}$  indicate the density and the mass fraction of the species  $s$  in the level  $l$ , respectively. The density of each species is computed as the sum of the densities of the single levels, thus  $\rho_s = \sum_l \rho_{s,l}$ , while the density of the mixture is  $\rho = \sum_s \rho_s$ . Note that  $\mathbf{V}_c = \sum_{s=1}^{N_s} \sum_{l=1}^{V_s} \rho D_s \nabla Y_{s,l}$  is a correction velocity to force the mass conservation [22].  $D_s$  is the diffusion coefficient of species  $s$  in the mixture. Binary diffusion and single-species viscosity coefficients

are calculated following Gupta's curve fits [23], whereas Eucken's formula is used to compute species conductivity (translational and vibrational). Mixing rules proposed by Mason and Saxena [24] and by Wilke [25] are employed to evaluate thermal conductivity and viscosity of the mixture, respectively, whereas a weighted harmonic mean is used for mixture diffusion coefficients. Both the thermochemical models implemented (namely, the multitemperature and the State-to-State models) employ the same algorithm for the computation of the transport properties. Anyway, in the temperature range reached in the considered test cases, transport properties calculated with the Gupta-Wilke-Eucken model do not present important deviations from more sophisticated models [26–28]. Lastly, the system is closed by solving the perfect gas equation of state:

$$p = \frac{\rho \mathcal{R} T}{\mathcal{M}} \quad (5)$$

where  $\mathcal{M}$  and  $\mathcal{R}$  are the mixture molar mass and the universal gas constant, respectively. For the sake of brevity, thermochemical models are provided in Appendix A and Appendix B.

## 2.2. Numerical scheme

90

The fluid dynamic solver is finite-volume based. Inviscid fluxes are discretized through the Steger-Warming flux-vector splitting scheme [29], combined with a second order MUSCL reconstruction in space. Gauss divergence theorem, with a linear interpolation, is applied for the evaluation of viscous fluxes.

Due to the large dimension and complexity of the chemical model, resulting in a large stiffness of the problem, the code efficiency is considerably improved by a splitting approach. In the first step, the homogeneous equations are solved and the conserved flow variables are advanced in time by using a step size  $\Delta t_f$  calculated on the basis of the CFL condition, as shown in [30] and Appendix E. An explicit third-order Runge–Kutta method is employed for time integration in order to provide sufficient temporal accuracy to capture the unsteady behavior of the flow [31]. In the second step, source terms are evaluated to describe

chemical phenomena and the inhomogeneous system of equations, given by

$$\int_{V_0} \frac{\partial}{\partial t} \mathbf{U} dV = \int_{V_0} \mathbf{W}(\mathbf{U}^{hom}) dV \quad (6)$$

95 must be integrated using a time step  $\Delta t_c = \Delta t_f/n$  and applying the Gauss–  
Seidel iterative scheme to solve at each time sub-step the system of nonlinear  
species continuity equations. The number  $n$  of sub-steps has been fixed to 4  
in the present work, having verified that 8 sub-steps provide the same results.  
More implementation details are given in [20, 21]. This approach was found  
100 suitable for the treatment of chemical terms [32]. Indeed, as it will be shown  
in the following, the results are perfectly comparable to those obtained by Hao  
et al. [10] with a coupled implicit algorithm. Moreover, an explicit algorithm,  
involving fewer floating point operations, is more suitable for GPUs implemen-  
tation (higher efficiency) with respect to an implicit approach requiring matrix  
105 inversion, especially for the StS model that presents more than 100 chemical  
equations.

### 3. Geometric configuration and flow conditions

The geometric configuration of the double-wedge is shown in figure 1, (the  
reference values used for the calculation are listed in table 1) where the blue  
110 lines reproduce the general shock structure. When the flow impacts on the  
first wedge, an oblique shock (OS) is formed: its structure mainly depends on  
the inclination  $\theta_1$  of the first wedge and can be predicted through the classical  
gas dynamics laws. Once the fluid reaches the second wedge, a bow shock  
(BS) develops. Its interaction with the OS generates a transmitted shock (TS)  
115 that, impinging on the surface, induces an adverse pressure gradient. As a  
consequence, a separation region (SR) and a separation shock (SS) appear,  
both moving along the wall of the first wedge. It is worth highlighting that for  
the considered value of  $\theta_2$ , the low enthalpy flow should become periodic after  
the separation region is completely developed [8].

120 Numerical simulations in 2D configuration have been performed for the low  
enthalpy (LE) and the high enthalpy (HE) regimes, characterized by different

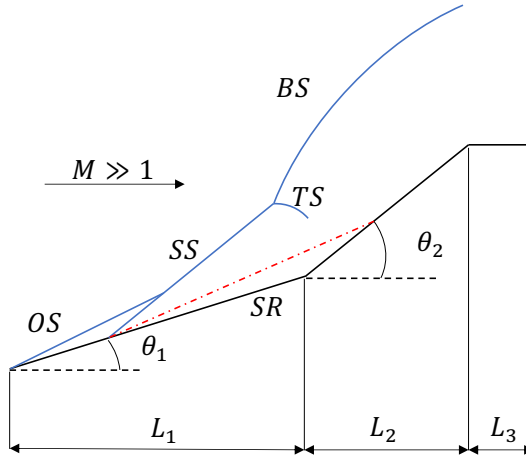


Figure 1: Sketch of the geometry (in black) and of the shock structure (in blue) of a double-wedge flow: separation region (SR, in red), oblique shock (OS), separation shock (SS), transmitted shock (TS), bow shock (BS).

Table 1: Reference values for the double-wedge geometry: lengths in meters and angles in degrees.

$\theta_1$	$\theta_2$	$L_1$	$L_2$	$L_3$
30	55	0.04399	0.01458	0.01082

free stream conditions, listed in table 2. The characteristic time  $\tau_c$  is the time needed by a particle to travel through the characteristic length  $L_c = L_1 + L_2$  ( $\approx 0.06$  m in the present case) where  $L_1$  and  $L_2$  are the horizontal projections of the two wedges [4], i.e.  $\tau_c = L_c/u_\infty$ . For both cases, the flow is laminar and the wall is non-catalytic and isothermal. The composition of the gas mixture does not affect the macroscopic quantities of the flow [33] with the exception of the gas temperature depending on the specific gas constant. Hence, the same free stream conditions have been used for both nitrogen and air mixtures. 125

The entire flow field is initialized with the free stream conditions. Symmetry 130

Table 2: Flow conditions for the low (LE) and high (HE) enthalpy regimes.  $\tau_c$  is the characteristic time as defined in Ref. [4].

Quantity	LE	HE
Mach number	7.11	7.14
Stagnation enthalpy [MJ/kg]	2.1	8.0
$u_\infty [m/s]$	1972	3812
$p_\infty [Pa]$	391	780
$T_{\infty,N_2} [K]$	168	691
$T_{\infty,Air} [K]$	191	710
$\rho_\infty [kg/m^3]$	0.007	0.0038
$\tau_c [\mu s]$	30.4	15.7
$T_w [K]$	300	300

boundary conditions are imposed along the stagnation streamline, while the no-slip boundary condition is used at the wall, as shown in fig. 2. A  $768 \times 384$  grid (see fig. 2) with the minimum wall normal spacing equal to  $5 \times 10^{-6}$  m, allows us to reproduce the results obtained by Hao et al. [10]. A grid convergence study is provided in Appendix D.

#### 4. Results

This section is dedicated to the discussion of the results and it is divided into two parts: in the first subsection, the periodic behavior of the flow is analyzed using the multitemperature Park model, underlining the influence of the flow regime. In the second subsection, thermochemical non-equilibrium effects are considered, discussing the results of both multitemperature and StS models. The analysis is carried out by collecting Schlieren images (density gradient magnitude contours), wall pressure and heat flux distributions that are compared with reference results [10].

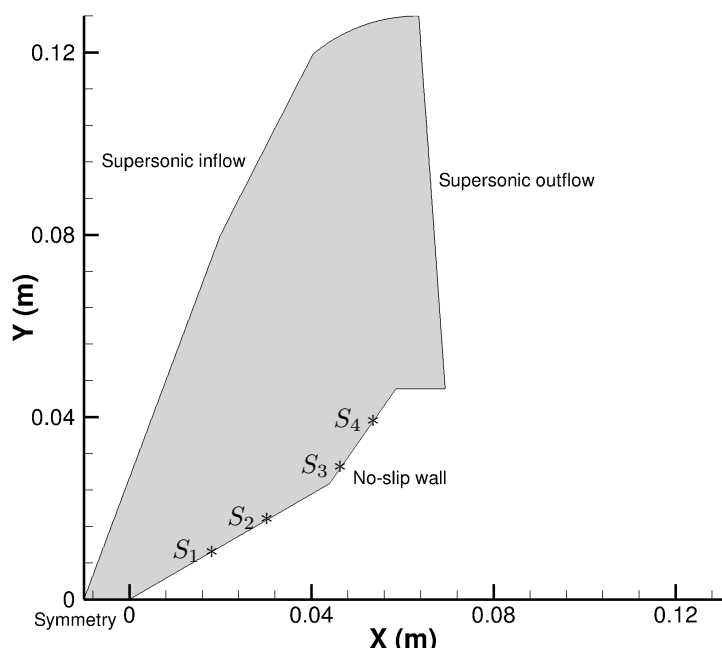


Figure 2: Computational domain. Stars are Eulerian markers for the observation stations. The  $x$  position of the stations are in the order (in meter):  $x_1 = 0.021993$ ,  $x_2 = 0.03299$ ,  $x_3 = 0.0503$ ,  $x_4 = 0.056607$

<sup>145</sup> 4.1. *Periodicity of the flow*

It has been shown by Durna and Celik [8] that in some cases the flow can be periodic. Specifically, they found that for nitrogen flow at LE regime non-stationarity takes place for values of  $\theta_2$  larger than 47 degrees. In the present work, the periodic behavior will be discussed for both nitrogen and air flows.  
<sup>150</sup> Moreover, the HE regime will be studied and the results will be compared with those of the LE regime.

To capture non-stationary phenomena, four stations have been selected to observe the time evolution of the local heat flux. The first two are placed on the first wedge, the other two on the second wedge, as shown in figure 2. Figure  
<sup>155</sup> 3 shows the heat flux trends in the four stations as function of the flow time (namely the simulation time normalized by  $\tau_c$ ), for the LE regime nitrogen test case. The present analysis is in agreement with the results obtained by Durna and Celik [8]: the periodic behavior is evident from the picture, even if one has to point out that most of the heat transfer occurs along the second  
<sup>160</sup> wedge, where oscillations are more pronounced (station  $S_4$ ). The amplitude of the oscillations in stations  $S_3$  and  $S_2$  are comparable and this is in agreement with their position, closer to the compression corner. Despite the axis scale, the periodicity of the heat flux can be observed also in station  $S_1$ , as shown in figure  
<sup>165</sup> 3(b). The periodicity of the flow can be related to the position of the transmitted shock with respect to the body: indeed, as also found by Durna and Celik [8], after the shock structure is established, the interaction between the transmitted shock and the wall plays a key role. When this shock does not impinge on any wedge, the flow reaches a steady state. For a better understanding of this phenomenon, four snapshots within the period of the low enthalpy nitrogen flow  
<sup>170</sup> have been captured, and are illustrated in figure 4. It is evident that, as soon as the transmitted shock impinges on the expansion corner, the unsteadiness is induced and the shock slips on the horizontal wall.

It deserves to be underlined that, given the low values of enthalpy (temperature), the flow can be considered frozen. A contour plot of the translational  
<sup>175</sup> temperature is provided in figure 5. The maximum value of the temperature

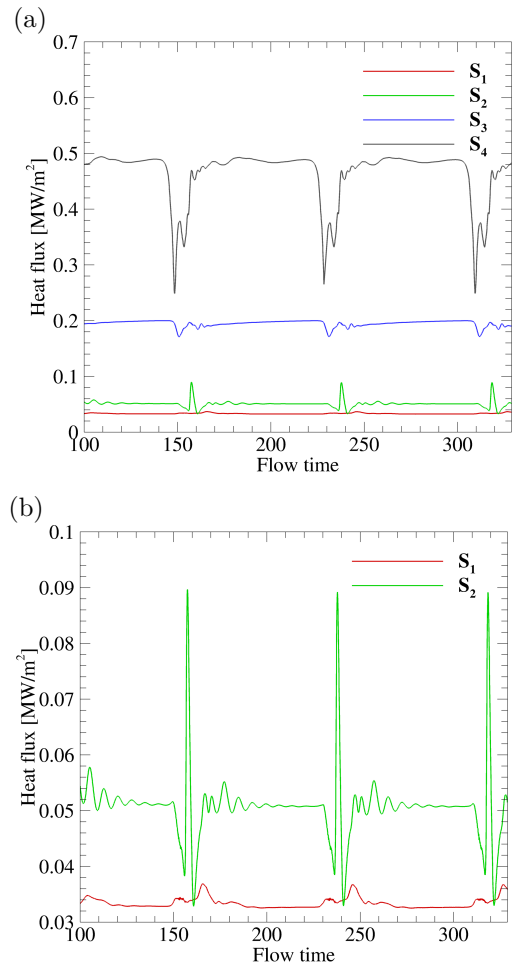


Figure 3: Heat flux distributions in time for the four stations in the nitrogen LE regime (a). Stations  $S_1$  and  $S_2$  (b).

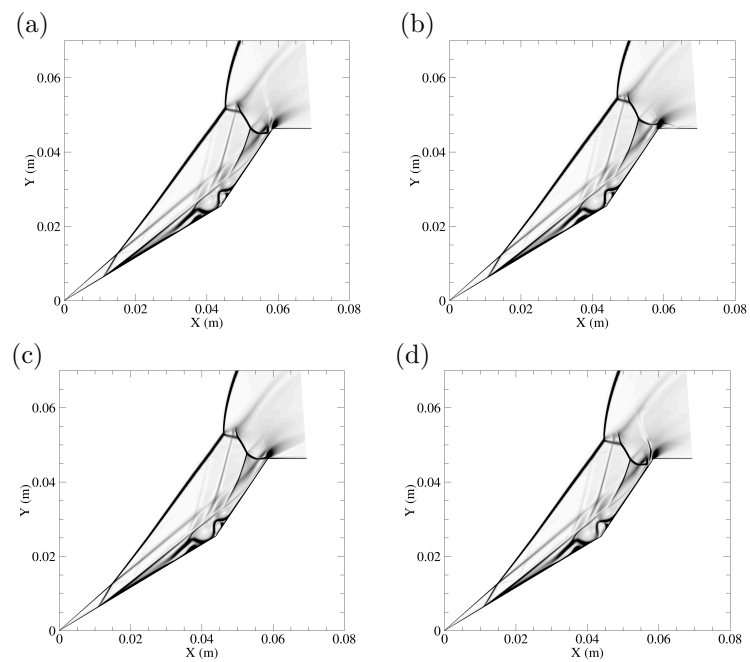


Figure 4: Schlieren of the low enthalpy nitrogen flow at different instants: (a) 148 flow times, (b) 181 flow times, (c) 214 flow times, (d) 230 flow times.

does not exceed 2000 K: indeed, it turned out from the simulations that  $Y_{N_2}$  is constant in time and  $Y_N$  is equal to zero (no nitrogen dissociation [11, 34]). Notice that, by comparing figures 1 and 5(a), one can distinguish the shock waves fronts. Moreover, the separation region is highlighted by the presence of vortex structures near the compression corner (figure 5(b)).

180

To complete the analysis of the LE regime, a comparison of the heat flux for the nitrogen and air mixtures at station  $S_4$  is illustrated in figure 6. The air mixture flow takes longer than nitrogen to reach the periodicity and also the period is larger: it is equal to 86 flow times ( $\approx 2.6$  ms) for the air mixture and to 80 flow times ( $\approx 2.4$  ms) for the nitrogen mixture. Therefore, being the simulation time the same (10 ms) for both cases, only two complete periods are captured in the range from 100 to 329 flow times in the air flow, while the third oscillation is only at beginning. As expected, the amplitudes of the oscillations are comparable in the two cases.

185

Differently from the LE case, in the HE one the flow asymptotically reaches a stationary regime. This is shown in figure 7 where the heat flux distributions in time at the four selected points are provided for the nitrogen and air flows, thus showing the influence of the flow conditions on the time behavior. It is worth noticing that in station  $S_1$  the heat transfer is larger for the air mixture, even though comparable values can be observed at the steady state. Figure 190  
8 shows a Schlieren contour at the steady state for the high enthalpy nitrogen flow: it is evident that the transmitted shock does not interact with the wall and consequently, in agreement with the previous discussion, the steady condition is reached. The analysis above extends to air flow and to HE regime the study of Durna and Celik [8]: it can be assessed that the periodic non-stationarity of 195  
the flow over double-wedges depends on the free stream flow conditions as well as on the geometrical configuration.

195

200

#### 4.2. High temperature effects

While in LE regime the equilibrium assumption is valid [2, 8], especially for nitrogen because of the large dissociation energy, in the HE regime, high 205

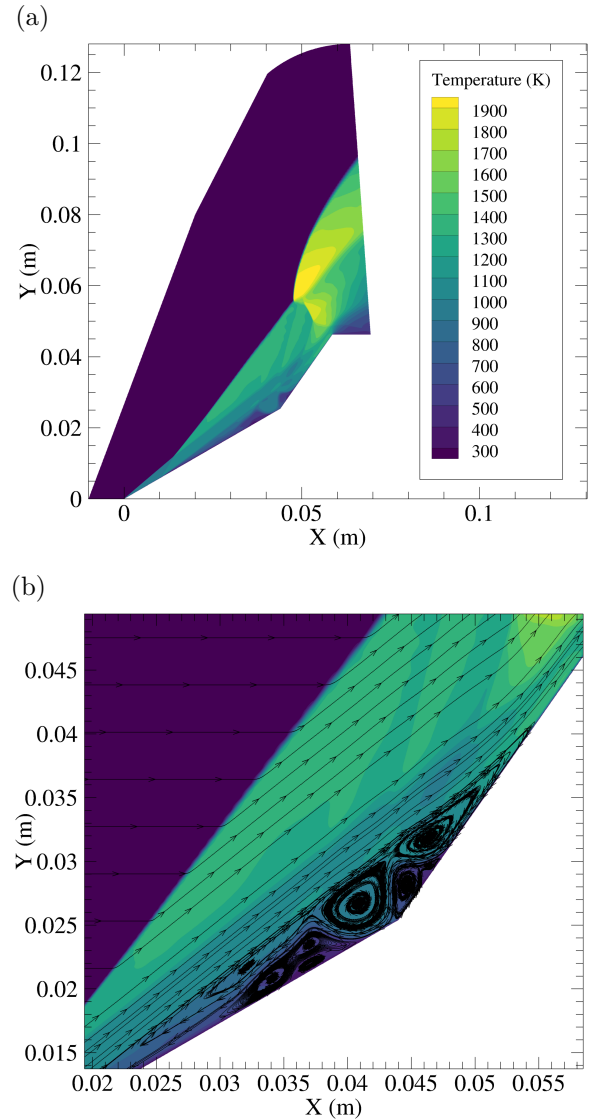


Figure 5: Contour of the translational temperature at  $t/\tau_c=329$  for nitrogen flow in LE regime  
(a). Close up of the compression corner with stream-traces visualization (b).

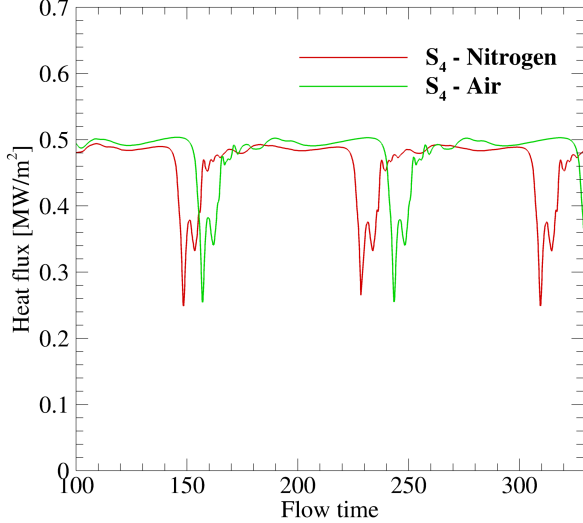


Figure 6: Trend of heat flux in station  $S_4$ : a comparison between nitrogen and air mixtures.

temperature effects are more relevant, with an impact on the macroscopic flow quantities, and have to be opportunely treated.

For this investigation, Schlieren contours, wall pressure and heat flux distributions have been collected at the same snapshots chosen by Hao et al. [10], namely 60, 120, 180 and 242  $\mu$ s, in the transient state.

210

#### 4.2.1. Nitrogen flow

The first analysis is carried out on the nitrogen flow. The initial mixture is exclusively composed of molecular nitrogen ( $Y_{N_2} = 1$  and  $Y_N = 0$ ). Figure 9 provides wall pressure and heat flux distributions at  $t = 242 \mu$ s. The trends obtained in the present work by employing Park model (green solid lines) show a good agreement with reference values [10], even if very small differences can be observed in the peak zone ( $\approx 56$  mm) probably due to a mismatch in the synchronization of origin of the time axis. From these results it emerges that the StS and multi-temperature models do not provide solutions with significant differences.

215

220

A comparison of the Schlieren images is shown in figure 10. As for the

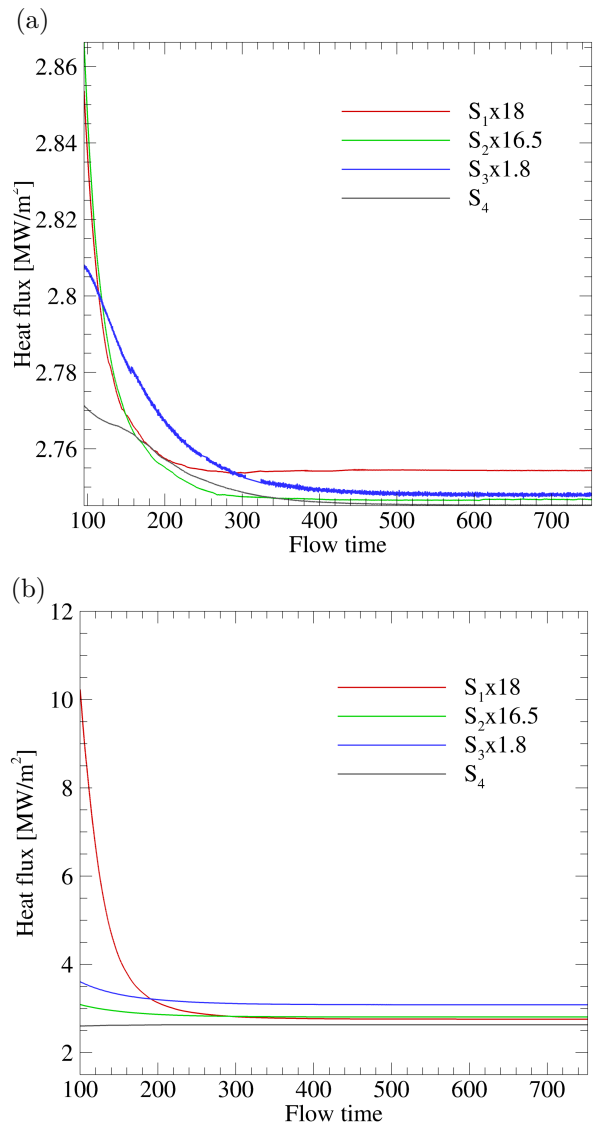


Figure 7: Heat flux distributions in time for the four stations: nitrogen (a) and air (b).

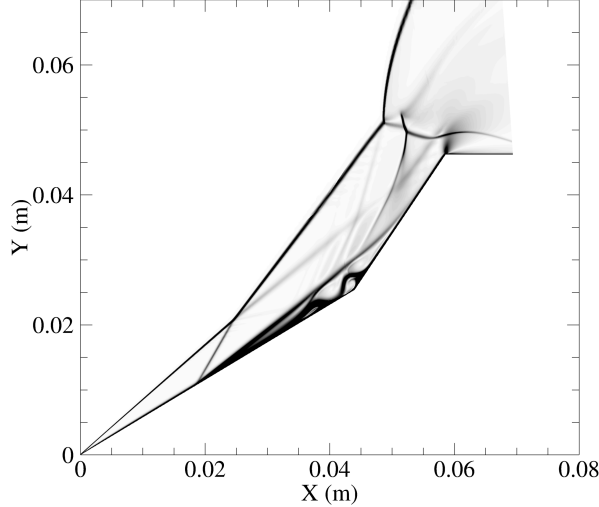


Figure 8: Schlieren of the high enthalpy nitrogen flow at the steady state ( $t = 0.01$  s).

wall quantities distributions, the contours of the density gradient magnitude obtained by the two models are very similar. In both cases, the separation region can be distinguished. In particular, it is evident its expansion in time along the first wedge, from the compression corner toward the leading edge, as also observed by Hao et al. (figure 6 of [10]). At  $t = 120 \mu\text{s}$  the oblique shock and the bow shock interact with each other, generating a transmitted shock and a separation shock, that induces the boundary layer separation. Over the time, the separation region extends more and more as observed at  $t = 180 \mu\text{s}$  and  $t = 242 \mu\text{s}$ .

Figure 11 illustrates the contours of the translational temperature and mass fraction of  $\text{N}_2$ . The values of the temperature are not sufficiently high to make nitrogen dissociate, being its mass fraction  $\approx 1$ . From tables C.3 and C.4 in Appendix C, one can notice that (for 1 GPU) the gain in terms of computational cost by employing the Park model with respect to the StS model is about 156. Hence, relying on these results, it can be assessed that the use of the StS model is not justified for this test case, since there are no dissociation phenomena nor

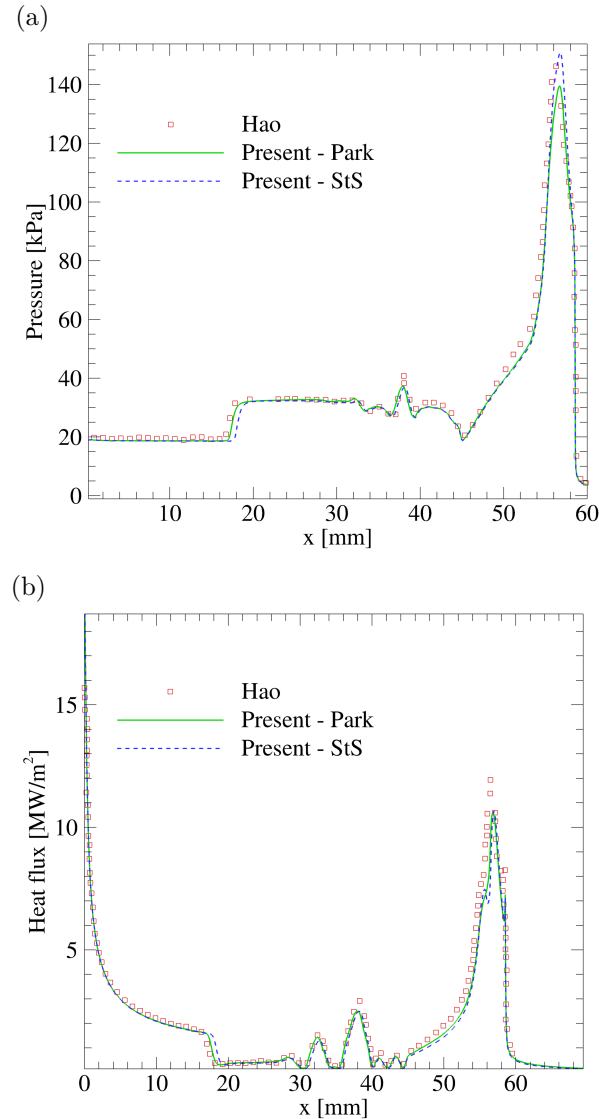


Figure 9: Wall distributions (present work and reference [10]) for HE nitrogen flow at  $t = 242 \mu\text{s}$  in terms of pressure (a) and heat flux (b).

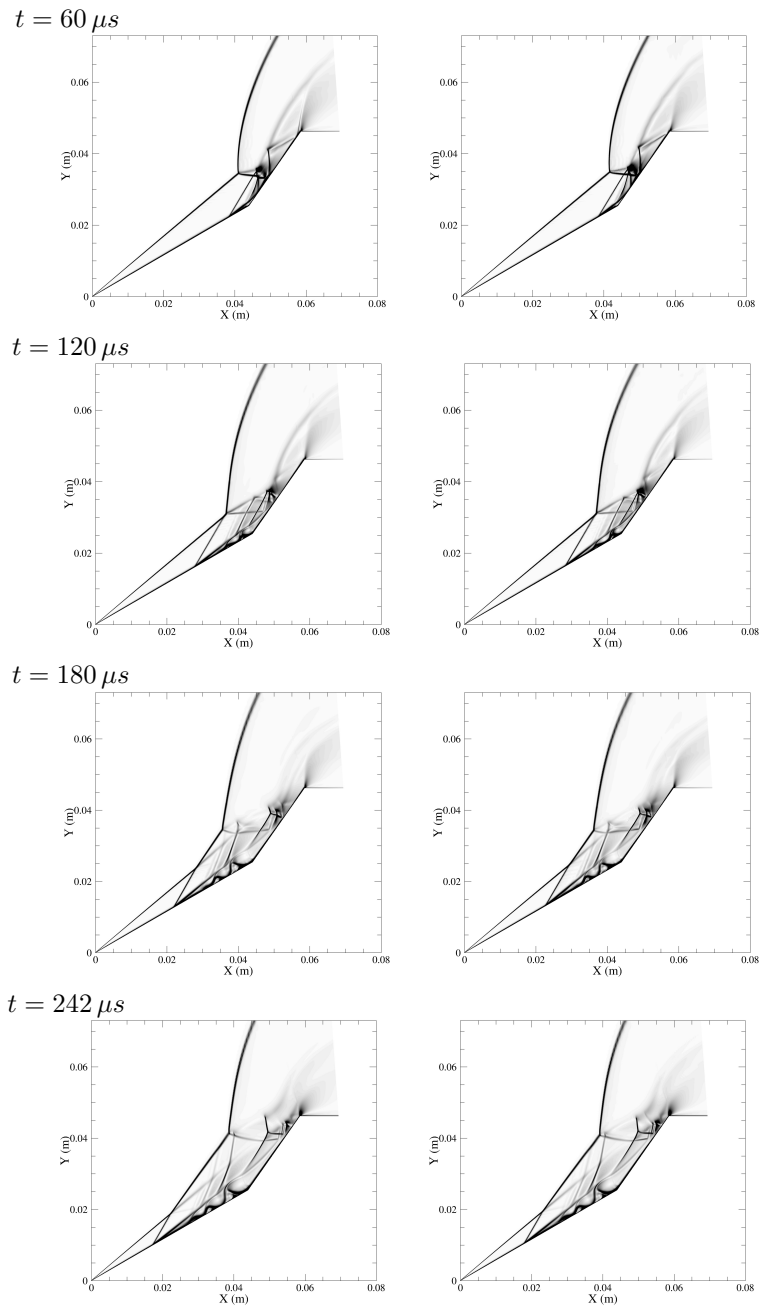


Figure 10: Schlieren for nitrogen at different instants: Park (left) and StS (right). Legend is omitted for a better view.

marked differences with respect to the Park model.

#### 4.2.2. Air flow

This subsection is devoted to the analysis of the air mixture flow at HE regime. The initial mixture is composed of molecular nitrogen (78%) and molecular oxygen (22%). In this case thermal non-equilibrium has a non negligible influence on the macroscopic quantities, mainly due to oxygen dissociation, becoming active at  $T = 2000$  K [11, 34]. The presence of oxygen atoms will lead to the formation of nitric oxide.

It should be pointed out that the distribution of wall quantities (see figure 12) calculated with the StS approach departs from the Park model in terms of extension of the separation region. By observing figure 12, it emerges that the general trend of pressure and heat flux is coherent with those provided in reference [10] and with the multi-temperature model, even if the position of the separation shock is further upstream. This is also confirmed by the Schlieren images in figure 13, perfectly in agreement with the Schlieren obtained by Hao et al. (figure 15 of [10]). The same behavior of the SWBLI of the nitrogen mixture can be observed for the air mixture, even if the extension of the separation region provided by the two models at the same instant appears different. Indeed, due to a smaller dissociation, the StS model solution provides stronger shocks (as confirmed by the pressure peak in figure 12) that, as a consequence, travel with a higher speed.

Figure 14 illustrates the contours of translational temperature and vibrational temperature of  $O_2$ , calculated with the two models. Differences can be observed in the vicinity of the bow shock, where StS predicts higher  $T_{v,O_2}$  and lower  $T$ .

In figure 15, the NO mass fraction calculated with StS and Park models are compared. A very sharp formation of NO has been calculated by the Park model, consequence of the overprediction of the oxygen dissociation. To better appreciate the difference in terms of mass fractions between the two models, profiles for  $Y_{O_2}$ ,  $Y_O$  and  $Y_{NO}$  have been extracted along a vertical section at

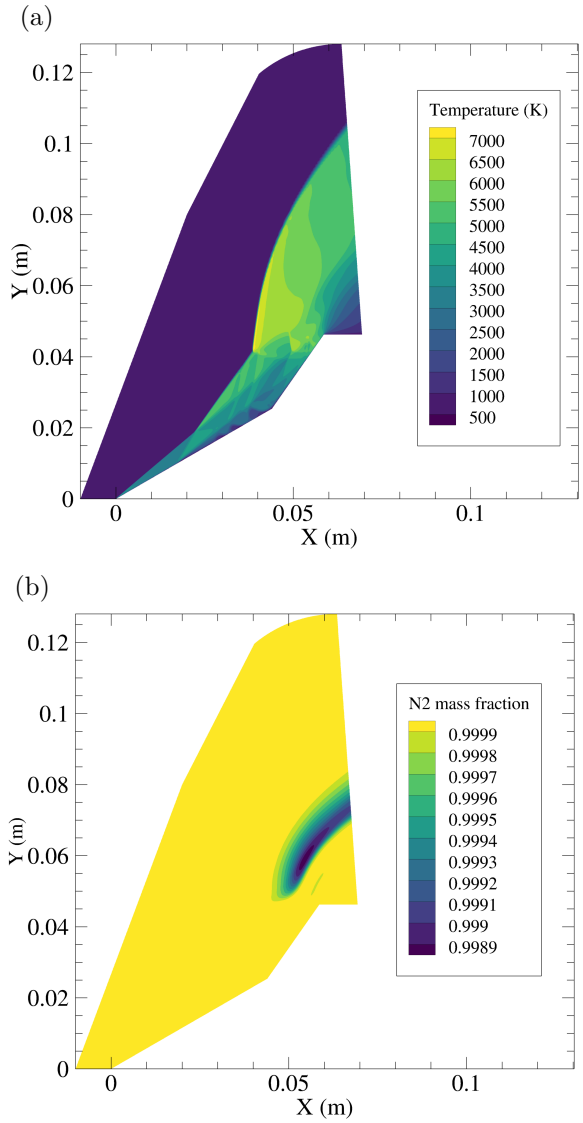


Figure 11: Contours of translational temperature (a) and N<sub>2</sub> mass fraction (b) at  $t = 242 \mu s$  (Park).

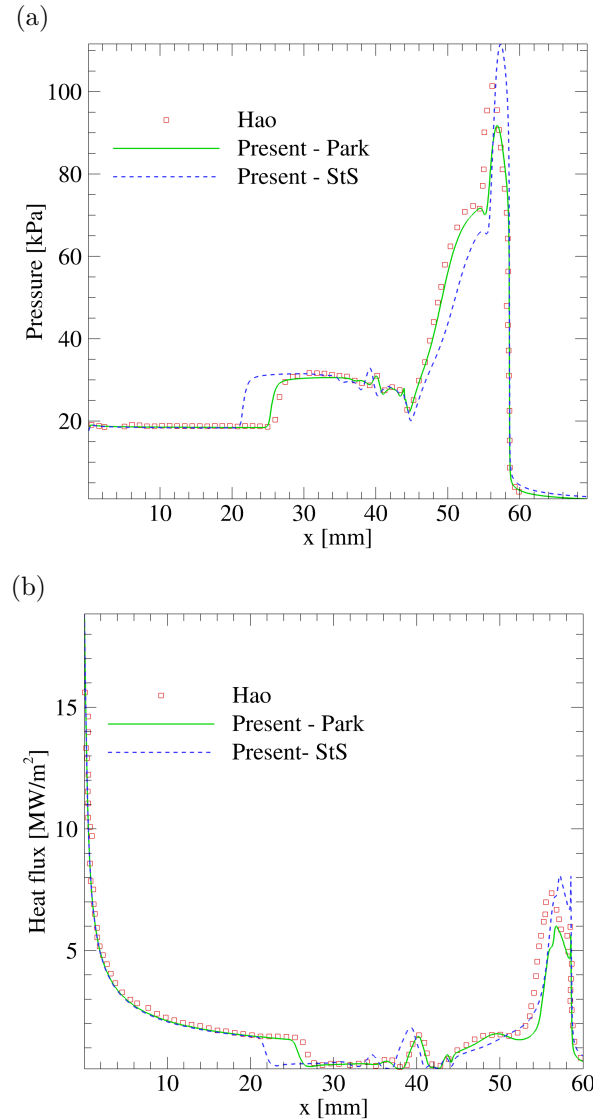


Figure 12: Wall distributions (present work and reference [10]) for HE air flow at  $t = 242 \mu s$  in terms of pressure (a) and heat flux (b).

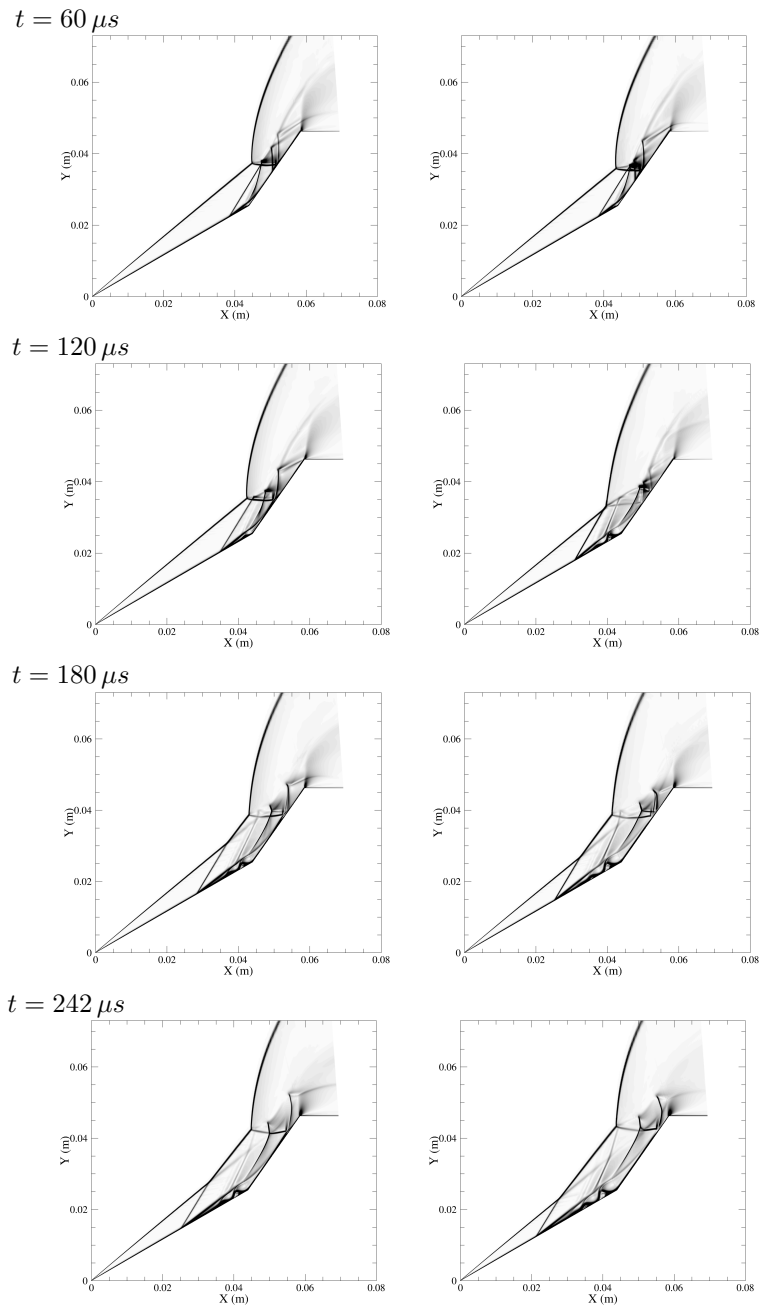


Figure 13: Schlieren for air at different instants: Park (left) and StS (right). Legend is omitted for a better view.

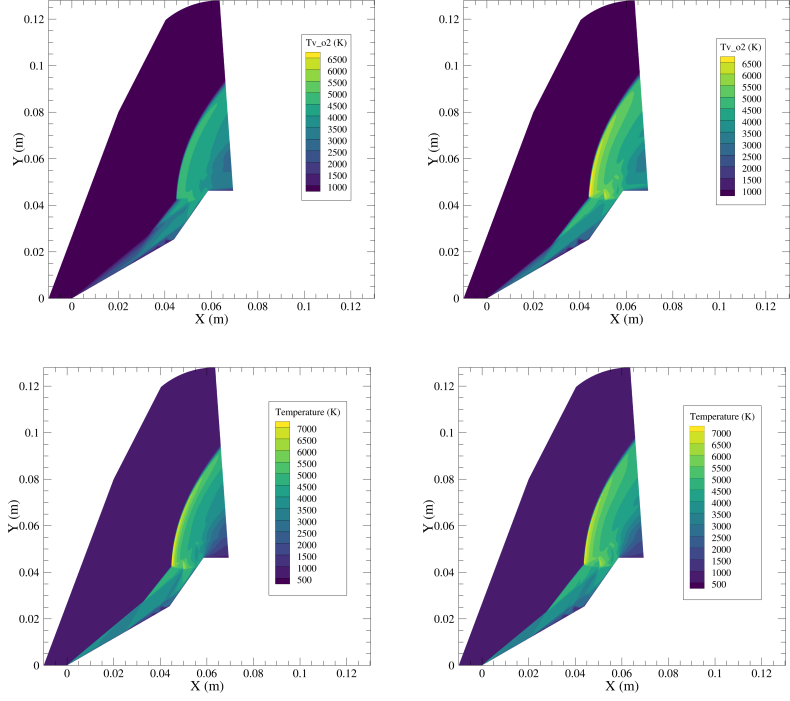


Figure 14: Contours of  $T_{v,O_2}$  (top) and  $T$  (bottom) in air at  $t = 242 \mu s$ : Park (left) and StS (right).

$x = 0.058 m$  ( $y_w = 0.0462 m$ ), from the wall to the free stream and shown in figure 16. The qualitative trend of the mass fraction are similar in the two models, even if the Park model results in higher dissociation and NO formation.

It is particularly interesting to compare the distributions of the levels obtained by the StS model with the Boltzmann ones calculated at the local vibrational temperature. To this purpose, six probe points have been chosen, shown in figure 17, and the comparison is reported in figure 18. One has to point out that in probes 3, 4 and 5, the assumption of a Boltzmann distribution is reasonable, with the exception of the highest levels whose populations would be overpredicted. These probe points are located in the subsonic zone, where the dissociation leads to an underpopulation of the most energetic levels. On the contrary, actual distributions in probes 1, 2 and 6 depart from the Boltzmann

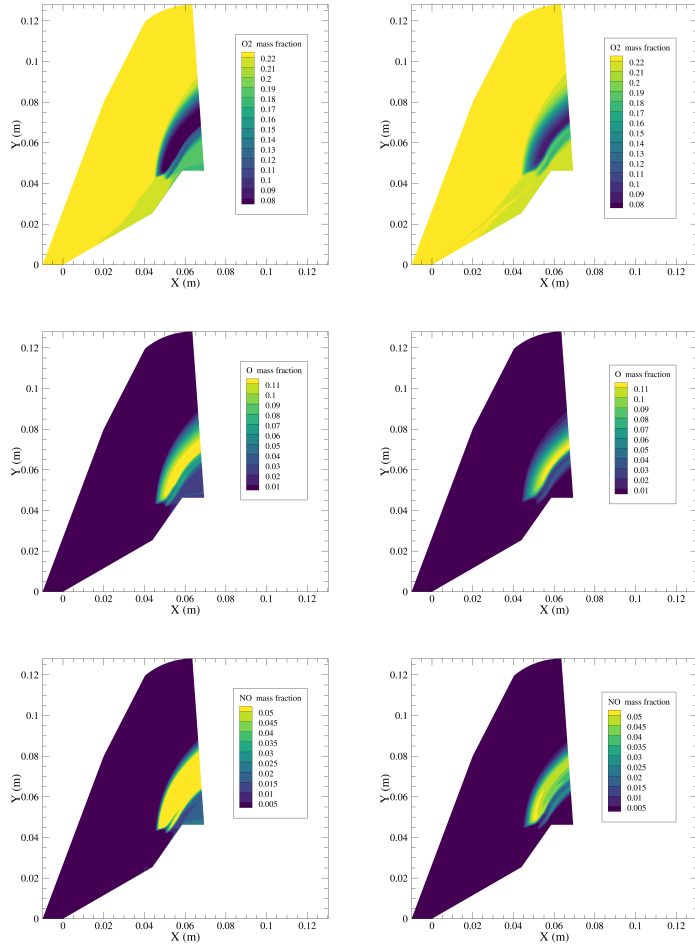


Figure 15: Contours of  $Y_{O_2}$ ,  $Y_O$ ,  $Y_{NO}$  in air at  $t = 242 \mu s$ : Park (left) and StS (right).

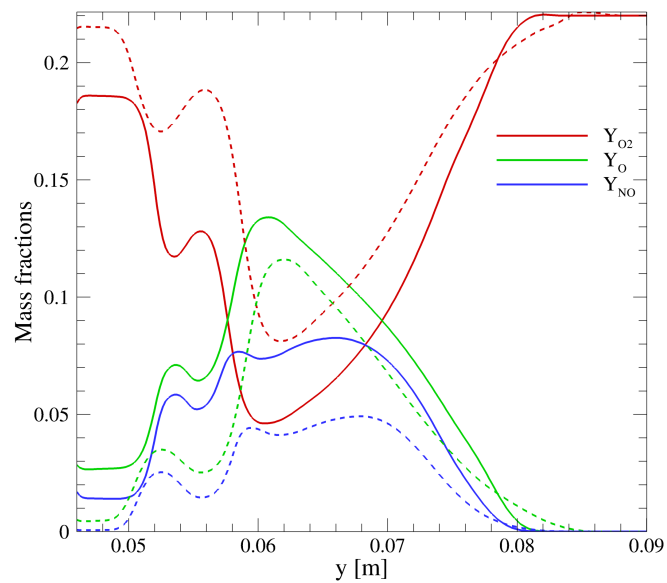


Figure 16: Mass fractions profiles along a vertical line in the section  $x = 0.058\text{ m}$  at  $t = 242\text{ }\mu\text{s}$ :  
Park (solid lines) and StS (dashed lines).

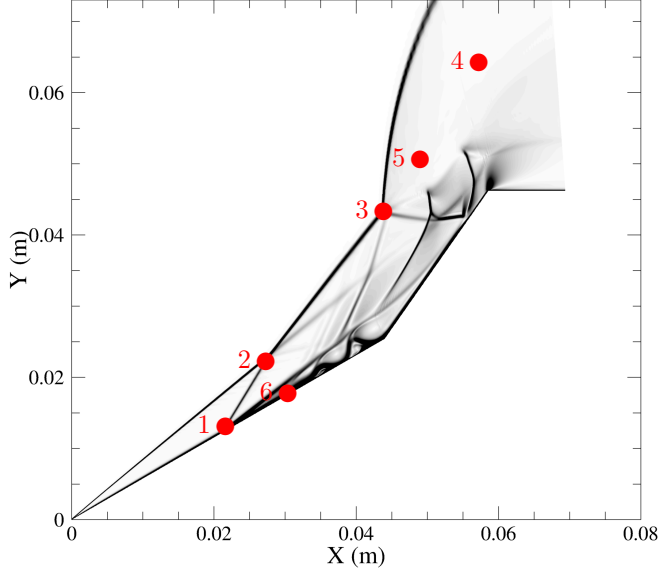


Figure 17: Probes along the separation shock to analyze levels distributions.

ones, especially for points 1 and 6 placed on the wall. The atomic recombination 280 causes important deviations from the Boltzmann distribution.

## 5. Conclusions

In this work, 2D numerical results have been presented for hypersonic flows over a double wedge. Two main topics have been investigated, namely, the non-stationary behavior of the flow and the high-temperature effects. It turned 285 out that for the LE flow conditions, thermochemical non-equilibrium does not influence the flow features; on the other hand, the flow becomes periodic after the separation region is completely developed. The composition of the mixture (nitrogen or air) just affects the period, whereas the amplitude of the oscillations is comparable for the two gases. 290

On the contrary, in the HE case the flow reaches a steady-state shock structure. The Park model shows a very good agreement with results of Hao et al.

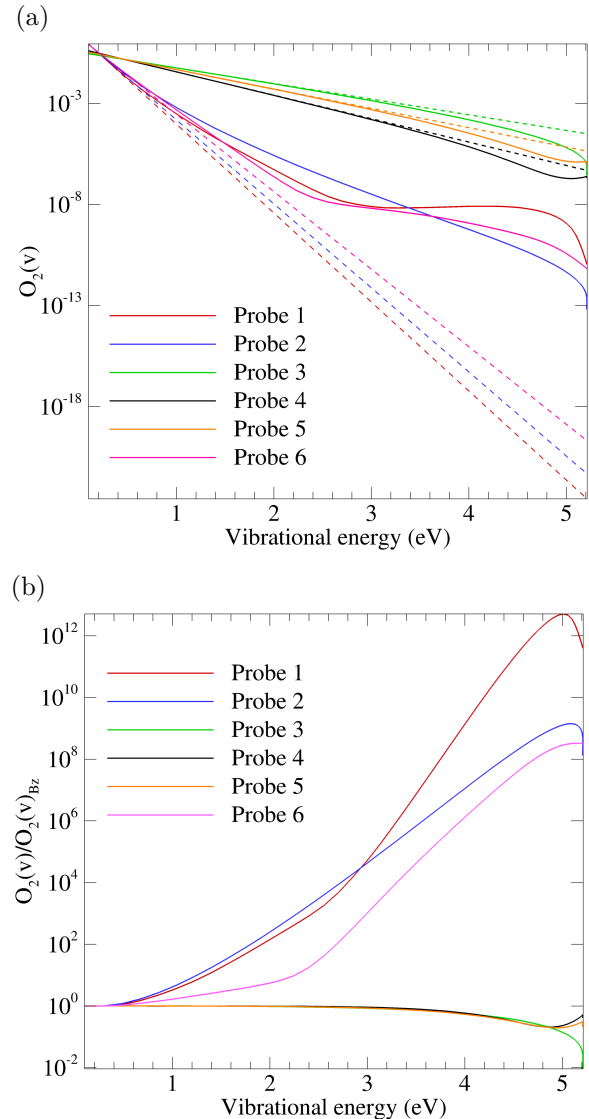


Figure 18: Population of  $\text{O}_2$  (solid lines are actual and dashed lines are Boltzmann distributions) in the probe points (a) and actual to Boltzmann ratio (b) at  $t = 242 \mu\text{s}$ .

[10] in terms of Schlieren images, pressure and heat flux distributions at the wall, for both nitrogen and air flows. The StS model provides similar results for nitrogen flow, while differences emerge for the case of air mixture flow. As expected, chemical phenomena are very sensitive to the model employed resulting in a stronger dissociation for the multitemperature model. 295

### Acknowledgment

D. Ninni, F. Bonelli and G. Pascazio were partially supported by the Italian Ministry of Education, University and Research under the Program Department of Excellence Legge 232/2016 (Grant No. CUP - D94I18000260001). The authors also acknowledge the CINECA award under the ISCRA initiative, for the availability of high performance computing resources and support under the allocations HP10CQ5D03 and HP10CGAD79. 300

### Appendix A. Park model

305

The multitemperature Park model accounts for a 5 species mixture and considers the following dissociation reactions:



and two NO exchange (Zeldovich) reactions:



Since each species can interact with any of the other ones, X represents a generic partner in the mixture, leading to 17 reactions. For the evaluation of chemical source terms  $\dot{\omega}_s$ , the law of mass action is employed,

$$\dot{\omega}_s = W_s \sum_{i=1}^{17} \nu_{is} RR_i \quad (\text{A.3})$$

where  $W_s$  is the molar weight of species  $s$ ,  $\nu_{is}$  is the difference between product and reactant stoichiometric coefficients of the species  $s$  in the reaction  $i$ . Rate coefficients of each reaction  $i$ ,  $RR_i$ , are evaluated as:

$$RR_i = k_{f,i} \prod_{s=1}^5 C_s^{\nu'_{is}} - k_{b,i} \prod_{s=1}^5 C_s^{\nu''_{is}} \quad (\text{A.4})$$

Here,  $\nu'_{is}$  and  $\nu''_{is}$  are reactant and product stoichiometric coefficients respectively,  $k_f$  and  $k_b$  are forward and backward rate coefficients and  $C_s$  is the concentration of species  $s$ . Following [11], Arrhenius formula is employed to evaluate forward coefficients,

$$k_{f,i} = A_i T_a^{n_i} \exp(-T_{d_i}/T_a) \quad (\text{A.5})$$

where  $T_a = \sqrt{T_v T}$  for dissociation reactions and  $T_a = T$  for NO exchange reactions. Parameters  $A_i$ ,  $n_i$  and  $T_{d_i}$  are given in [11] for dissociation reactions and in [35] for NO exchange reactions. The following expression is used to evaluate equilibrium constant:

$$K_{eq,i} = \exp[A_1(T_a/10000)+A_2+A_3 \ln(10000/T_a)+A_4 (10000/T_a)+A_5 (10000/T_a)^2] \quad (\text{A.6})$$

with coefficients given in [11]. Finally, backward rate coefficients are computed as follows:

$$k_{b,i} = k_{f,i}/K_{eq,i} \quad (\text{A.7})$$

Concerning the vibrational source terms of molecules  $\dot{\omega}_{vib,m}$ , two contributions are considered. Specifically,  $\dot{\omega}_{vib,m}$  can be decomposed in the collisional ( $\dot{\omega}_{LT,m}$ ) and chemical ( $\dot{\omega}_{chem,m}$ ) parts. This distinction is needed to provide an appropriate formulation of the total energy.

The collisional contribution  $\dot{\omega}_{LT,m}$  represents the energy transfer between translational and vibrational modes, and is modeled by the Landau-Teller equation:

320

$$\dot{\omega}_{LT,m} = \rho_m \frac{\varepsilon_{vib,m}(T) - \varepsilon_{vib,m}(T_v)}{\tau_m} \quad (\text{A.8})$$

where  $\tau_m$  is the relaxation time. It is immediate to verify that in the case of thermal equilibrium ( $T = T_v$ ) this contribution is null. As first approximation, it is evaluated through Millikan-White expression [11, 35], that reads:

$$\tau_{m,X}^{MW} = \frac{p_{atm}}{p} \exp \left[ A_{m,X} \left( T^{-1/3} - B_{m,X} \right) - 18.42 \right] \quad (\text{A.9})$$

It accounts for the collision of the molecule  $m$  with a generic partner X. The coefficients  $A_{m,X}$  and  $B_{m,X}$  can be evaluated following simple expressions given in [36]: specific values of this work are reported in [35]. Nevertheless, for temperatures above 5000 K, the prediction of the relaxation time obtained by using Millikan-White expression does not well reproduce experimental results [11, 35, 37], since it does not account for the limits in collision cross sections. To overcome this drawback, Park proposed a correction in the evaluation of  $\tau_m$  [11], taking into account the effective excitation cross section as

$$\tau_{m,X}^c = \frac{1}{N_m \sigma \sqrt{\frac{8\mathcal{R}T}{\pi \mu_{m,X}}}} \quad (\text{A.10})$$

$\mathcal{R}$  being the universal gas constant,  $N_m$  the number density of molecule  $m$ ,  $\sigma$  the effective excitation cross section equal to  $3 \cdot 10^{-17} (50000/T^2) \text{ cm}^2$  [35] and  $\mu_{m,X} = W_m W_X / (W_m + W_X)$  the equivalent molecular weight of two colliding particles.

335

Hence, the relaxation time for the collision between a molecule and a generic partner X is given by  $\tau_{m,X} = \tau_{m,X}^{MW} + \tau_{m,X}^c$  and its mean value is evaluated through a weighted harmonic average:

$$\frac{1}{\tau_m} = \frac{1}{N_t} \sum_{s=1}^{N_s} \frac{N_s}{\tau_{m,X}} \quad (\text{A.11})$$

where  $N_t$  is the total number density, while  $N_s$  is the number density of the species  $s$ .

The second contribution of the vibrational source terms is  $\dot{\omega}_{chem,m}$ , that takes into account the influence of the dissociation on the vibrational energy. In this work, the harmonic oscillator model is employed, thus the energy exchanged in dissociation process is equally divided in vibrational and translational degrees of freedom [11]:

$$\dot{\omega}_{chem,m} = \frac{D_m}{2} \dot{\omega}_m \quad (\text{A.12})$$

where  $D_m$  is the dissociation energy per unit mass of molecule  $m$ . Finally, vibrational temperatures are evaluated as follows:

$$\varepsilon_{vib,m} = \frac{R_m \theta_m}{\exp(\theta_m/T_v) - 1} \quad (\text{A.13})$$

where  $R_m$  is the gas constant of molecule  $m$ ,  $\theta_m$  is the characteristic vibrational temperature of molecule  $m$ . Following [11], these are equal to 3393 K, 2273 K and 2739 K for N<sub>2</sub>, O<sub>2</sub> and NO respectively.

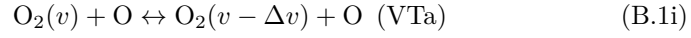
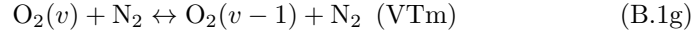
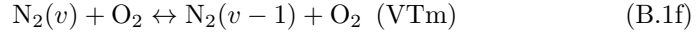
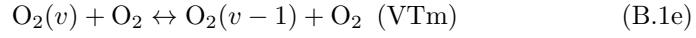
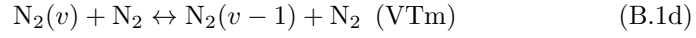
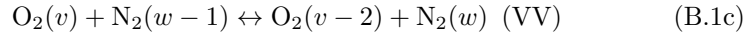
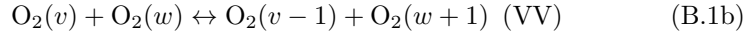
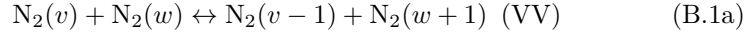
## Appendix B. State-to-state model

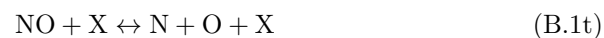
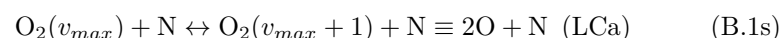
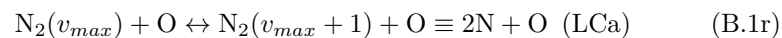
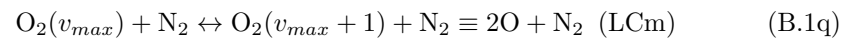
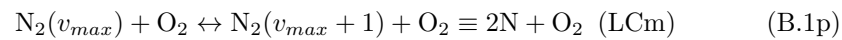
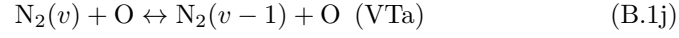
The multitemperature model accounts for thermochemical non-equilibrium in high enthalpy flows, but it is basically devoted to the fluid dynamics aspects. Concerning the kinetic properties, the assumption of a Boltzmann distribution is not always suitable and it can be responsible for large deviations of the rate coefficients from the Arrhenius law [38]. Since the energy levels are no longer sparsely populated, their distribution must be modeled by following a non-Boltzmann law, thus considering all the elementary processes contributing to the vibrational relaxation.

In this scenario, a state-to-state approach can be employed to provide the distribution of all internal states of the mixture. Nevertheless, this approach is time consuming since it accounts for all the vibrational levels of N<sub>2</sub> ( $V_{N_2} = 68$ )

and O<sub>2</sub> ( $V_{O_2} = 47$ ), whereas only the ground state is considered for NO, N and O.

The elementary processes contributing to the vibrational relaxation are due to vibration-vibration (VV) and vibration-translation by molecules (VTm) and by atoms (VTa) energy transfer. Moreover, dissociation-recombination by molecules (DRm) and by atoms (DRa) processes are involved, that are substituted by ladder climbing approach (LC) when data for direct dissociation model are missing. Finally, NO dissociation and Zeldovich reactions are considered. All these processes are here summarized:





As before,  $X$  is a generic partner among the species of the mixture, whereas  $v$  and  $w$  are generic vibrational levels. The total vibrational energy per unit mass is defined as follows:

$$\varepsilon_{vib} = \frac{1}{\rho} \sum_{s=1}^{N_s} \sum_{l=1}^{V_s} \rho_{s,l} \varepsilon_{s,l} \quad (\text{B.2})$$

$\rho_{s,l}$  and  $\varepsilon_{s,l}$  being the density and the vibrational energy of the species  $s$  in the vibrational level  $l$  ( $V_s$  is the total number of levels of the species  $s$ ). 375

Concerning the vibrational temperature, the classical harmonic oscillator model can not be applied. Nevertheless, low energy levels approximately follow a Boltzmann distribution, thus providing the vibrational temperature (from the first two levels) as: 380

$$T_{v,m} = \frac{W_m(\varepsilon_{m,2} - \varepsilon_{m,1})}{R \ln \left( \frac{\rho_{m,1}}{\rho_{m,2}} \right)} \quad (\text{B.3})$$

### Appendix C. GPU clustering

All the calculations have been performed on MARCONI100 machine (CINECA), that is provided of NVIDIA Volta V100 GPUs, Nvlink 2.0 (16GB). At the first stage, a performance analysis was carried out to define the optimum number of GPUs to be used. Table C.3 summarizes the computational costs to perform 20 iterations using Park model (times in seconds). Notice that they refer to both nitrogen and air mixture, since the total amount of routine calls is the same. 385

GPUs	Time [s]
1 GPU	0.4
2 GPUs	0.24
4 GPUs	0.21

Table C.3: Execution time for Park model.

From table C.3, it emerges that the scalability is not ideal: indeed, it has

been already shown in previous works that a better scalability is encountered  
 390 when employing the StS model [21].

The same analysis has been carried out for the StS model. Table C.4 summarizes the computational costs to perform 20 iterations for both nitrogen and air flows (times in seconds). In this case, it makes sense to distinguish them since for nitrogen flows one can by-pass some calculation involving oxygen reactions.

GPUs	Time N <sub>2</sub> [s]	Time Air [s]
1 GPU	62.4	200
2 GPUs	32.2	103.7
4 GPUs	16.4	53
8 GPUs	4.4	9.1
16 GPUs	2.5	4.9
32 GPUs	1.9	3.8

Table C.4: Execution time for StS model.

395 The scalability is more than linear when using up to 16 GPUs.

#### Appendix D. Mesh independence analysis

The grid employed to perform all the simulations is composed of  $768 \times 384$  cells. This has been verified to ensure mesh independent results, according to the refinement study carried out using two more grids, containing  $512 \times 256$  and  
 400  $1024 \times 512$  cells. The analysis has been performed for the high enthalpy air flow; figure D.19 shows the corresponding heat flux distributions.

Relying on these results, the medium mesh has been chosen for the simulations.

#### Appendix E. Time step independence analysis

405 Vatansever and Celik [9] have shown the influence of the time step size on the steady solution of the high enthalpy regime. It can be even more interesting

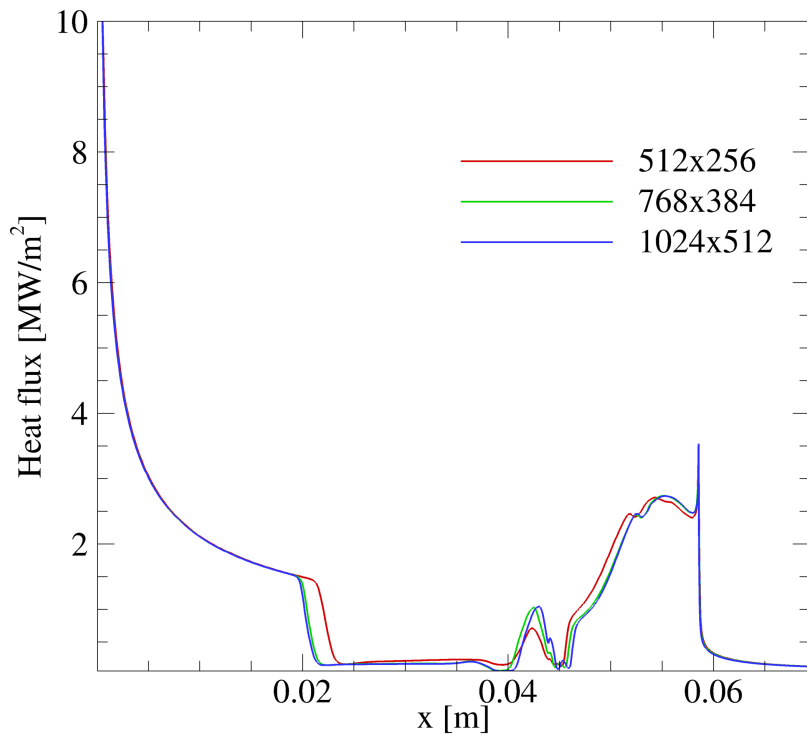


Figure D.19: Wall heat flux trend at the steady state (high enthalpy air flow) for 3 refinement levels of the mesh.

to analyze the time step size independence for the low enthalpy regime due to its periodic behavior. In this study, the computation of the time step size is based on the convective terms [30] and in cell  $(i, j)$  it reads:

$$\Delta t_{i,j} = \frac{\text{CFL } V_{i,j}}{|\mathbf{u}_{i,j} \cdot \bar{\mathbf{S}}_i| + |\mathbf{u}_{i,j} \cdot \bar{\mathbf{S}}_j| + c_{i,j} (\bar{S}_i + \bar{S}_j)} \quad (\text{E.1})$$

410 where  $V_{i,j}$  is the volume of the cell, whereas  $\mathbf{u}_{i,j}$  and  $c_{i,j}$  are the velocity vector  
 and the speed of sound in the cell, respectively.  $\bar{\mathbf{S}}_i$  and  $\bar{\mathbf{S}}_j$  represent the average  
 values of the normal vectors of the faces of the cell, whereas  $\bar{S}_i$  and  $\bar{S}_j$  are their  
 surface values. Since the flow is unsteady, a global time stepping approach is  
 415 used: the flow variables are advanced in time with the minimum  $\Delta t$  among  
 those evaluated in each cell.  $CFL$  is the Courant number, that is kept constant  
 in the simulations. By imposing  $CFL = 0.05$ , the time step size is of the order  
 of  $10^{-10}$  s. In the time step size independence study, the CFL number has been  
 halved and the simulation restarted from a certain instant ( $5 \times 10^{-3}$  s). Figure  
 420 E.20, providing the heat flux distribution in the station  $S_4$  for the low enthalpy  
 nitrogen flow, shows that time step independent solution is achieved.

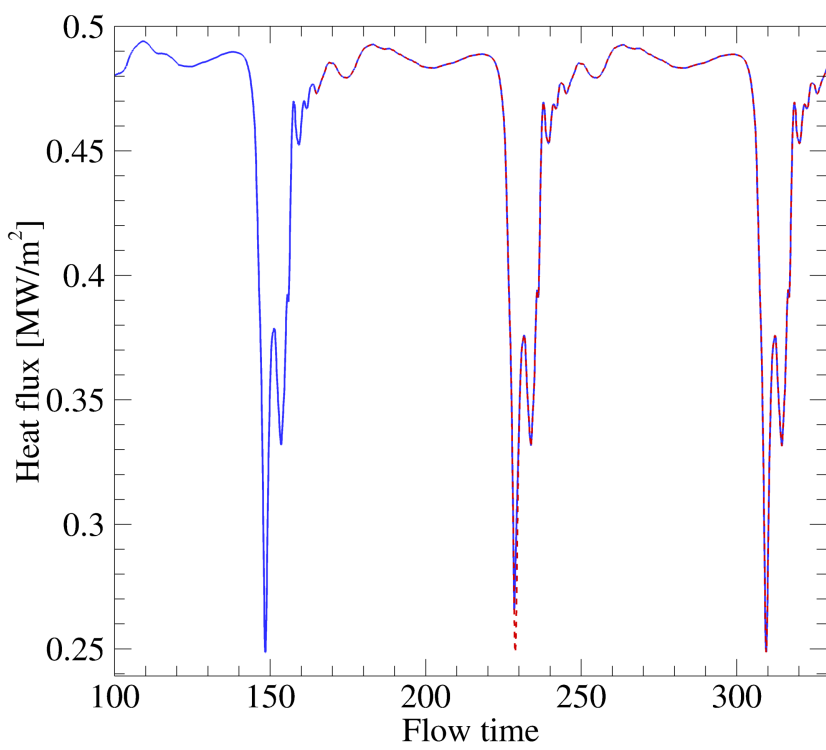


Figure E.20: Heat flux trend in station  $S_4$  for the low enthalpy nitrogen flow when  $CFL = 0.05$  (solid blue) and  $CFL = 0.025$  (dashed red).

## References

- [1] J. J. Bertin, R. M. Cummings, Fifty years of hypersonics: where we've been, where we're going, *Progress in Aerospace Sciences* 39 (6-7) (2003) 511–536.
- 425 [2] J. D. Reinert, G. V. Candler, J. R. Komives, Simulations of unsteady three-dimensional hypersonic double-wedge flow experiments, *AIAA journal* 58 (9) (2020) 4055–4067.
- [3] A. Swantek, J. Austin, Flowfield establishment in hypervelocity shock-wave/boundary-layer interactions, *AIAA Journal* 53 (2) (2015) 311–320.
- 430 [4] D. Knight, O. Chazot, J. Austin, M. A. Badr, G. Candler, B. Celik, D. de Rosa, R. Donelli, J. Komives, A. Lani, et al., Assessment of predictive capabilities for aerodynamic heating in hypersonic flow, *Progress in Aerospace Sciences* 90 (2017) 39–53.
- [5] D. de Rosa, G. Pezzella, R. S. Donelli, A. Viviani, Flap effectiveness appraisal for winged re-entry vehicles, *Acta Astronautica* 122 (2016) 175–184.
- 435 [6] G. Shovev, G. Oblapenko, O. Kunova, M. Mekhonoshina, E. Kustova, Validation of vibration-dissociation coupling models in hypersonic non-equilibrium separated flows, *Acta Astronautica* 144 (2018) 147–159.
- [7] F.-Y. Zuo, S.-L. Hu, Thermochemical non-equilibrium effects on aerothermodynamic prediction of laminar double-cone flow, *Acta Astronautica* 182 (2021) 179–188.
- 440 [8] A. Durna, B. Celik, Time-periodic shock interaction mechanisms over double wedges at mach 7, *Shock Waves* 29 (3) (2019) 381–399.
- [9] D. Vatansever, B. Celik, Unsteady shock interaction mechanisms of high enthalpy reacting flows over double wedges at mach 7, *Physics of Fluids* 33 (5) (2021) 056110.

- [10] J. Hao, C.-Y. Wen, J. Wang, Numerical investigation of hypervelocity shock-wave/boundary-layer interactions over a double-wedge configuration, International Journal of Heat and Mass Transfer 138 (2019) 277–292.
- [11] C. Park, Nonequilibrium hypersonic aerothermodynamics (1989). 450
- [12] M. Capitelli, R. Celiberto, G. Colonna, F. Esposito, C. Gorse, K. Hassouni, A. Laricchiuta, S. Longo, Fundamentals Aspects of Plasma Chemical Physics: Kinetics, Springer, New York, 2016.
- [13] G. Colonna, F. Bonelli, G. Pascazio, Impact of fundamental molecular kinetics on macroscopic properties of high-enthalpy flows: The case of hypersonic atmospheric entry, Physical Review Fluids 4 (3) (2019) 033404. 455
- [14] F. Bonelli, G. Pascazio, G. Colonna, Effect of finite-rate catalysis on wall heat flux prediction in hypersonic flow, Phys. Rev. Fluids 6 (2021) 033201.  
doi:10.1103/PhysRevFluids.6.033201.  
URL <https://link.aps.org/doi/10.1103/PhysRevFluids.6.033201> 460
- [15] M. Capitelli, G. Colonna, A. D’Angola, Fundamental aspects of plasma chemical physics, Vol. 66, Springer, 2012.
- [16] I. Armenise, M. Capitelli, G. Colonna, G. Gorse, Nonequilibrium vibrational kinetics in the boundary layer of re-entering bodies, Journal of thermophysics and heat transfer 10 (3) (1996) 397–405. 465
- [17] G. Colonna, M. Capitelli, Electron and vibrational kinetics in the boundary layer of hypersonic flow, Journal of thermophysics and heat transfer 10 (3) (1996) 406–412.
- [18] I. Armenise, M. Barbato, M. Capitelli, E. Kustova, State-to-state catalytic models, kinetics, and transport in hypersonic boundary layers, Journal of thermophysics and heat transfer 20 (3) (2006) 465–476. 470
- [19] M. Tuttafesta, G. Colonna, G. Pascazio, Computing unsteady compressible flows using roe’s flux-difference splitting scheme on gpus, Computer Physics Communications 184 (6) (2013) 1497–1510.

- 475 [20] M. Tuttafesta, G. Pascazio, G. Colonna, Multi-gpu unsteady 2d flow simulation coupled with a state-to-state chemical kinetics, Computer Physics Communications 207 (2016) 243–257.
- 480 [21] F. Bonelli, M. Tuttafesta, G. Colonna, L. Cutrone, G. Pascazio, An mpi-cuda approach for hypersonic flows with detailed state-to-state air kinetics using a gpu cluster, Computer Physics Communications 219 (2017) 178–195.
- [22] K. K.-y. Kuo, R. Acharya, Fundamentals of turbulent and multiphase combustion, John Wiley & Sons, 2012.
- 485 [23] R. N. Gupta, K.-P. Lee, R. A. Thompson, J. M. Yos, A review of reaction rates and thermodynamic and transport properties for an 11-species air model for chemical and thermal nonequilibrium calculations to 30000 k (1990).
- [24] E. Mason, S. Saxena, Approximate formula for the thermal conductivity of gas mixtures, The Physics of fluids 1 (5) (1958) 361–369.
- 490 [25] C. Wilke, A viscosity equation for gas mixtures, The journal of chemical physics 18 (4) (1950) 517–519.
- [26] E. Kustova, On the simplified state-to-state transport coefficients, Chemical Physics 270 (1) (2001) 177–195.
- 495 [27] T. E. Magin, G. Degrez, Transport algorithms for partially ionized and unmagnetized plasmas, Journal of computational Physics 198 (2) (2004) 424–449.
- [28] M. Capitelli, G. Colonna, C. Gorse, A. d’Angola, Transport properties of high temperature air in local thermodynamic equilibrium, The European Physical Journal D-Atomic, Molecular, Optical and Plasma Physics 11 (2) (2000) 279–289.

- [29] J. L. Steger, R. Warming, Flux vector splitting of the inviscid gasdynamic equations with application to finite-difference methods, *Journal of computational physics* 40 (2) (1981) 263–293.
- [30] C. Hirsch, Numerical computation of internal and external flows: The fundamentals of computational fluid dynamics, Elsevier, 2007. 505
- [31] G.-S. Jiang, C.-W. Shu, Efficient implementation of weighted eno schemes, *Journal of computational physics* 126 (1) (1996) 202–228.
- [32] J. G. Verwer, Gauss-seidel iteration for stiff odes from chemical kinetics, *SIAM Journal on Scientific Computing* 15 (5) (1994) 1243–1250.
- [33] A. Swantek, J. Austin, Heat transfer on a double wedge geometry in hypervelocity air and nitrogen flows (2012) 284. 510
- [34] J. D. Anderson Jr, Hypersonic and high-temperature gas dynamics, American Institute of Aeronautics and Astronautics, 2006.
- [35] C. Park, Review of chemical-kinetic problems of future nasa missions. i-earth entries, *Journal of Thermophysics and Heat transfer* 7 (3) (1993) 515 385–398.
- [36] R. C. Millikan, D. R. White, Systematics of vibrational relaxation, *The Journal of chemical physics* 39 (12) (1963) 3209–3213.
- [37] C. Park, Two-temperature interpretation of dissociation rate data for n<sub>2</sub> and o<sub>2</sub>, in: 26th Aerospace Sciences Meeting, 1988, p. 458. 520
- [38] G. Colonna, M. Tuttafesta, M. Capitelli, D. Giordano, Non-arrhenius no formation rate in one-dimensional nozzle airflow, *Journal of thermophysics and heat transfer* 13 (3) (1999) 372–375.